Extreme Mechanics Letters 72 (2024) 102246

Contents lists available at ScienceDirect

Extreme Mechanics Letters

journal homepage: www.elsevier.com/locate/eml

Harnessing centrifugal and Euler forces for tunable buckling of a rotating *elastica*

Eduardo Gutierrez-Prieto [a], Michael Gomez [a,b], Pedro M. Reis [a,*]

[a] Flexible Structures Laboratory, Institute of Mechanical Engineering, École Polytechnique Fédérale de Lausanne (EPFL), 1015 Lausanne, Switzerland
[b] Department of Engineering, King's College London, Strand, London WC2R 2LS, United Kingdom

ARTICLE INFO

Keywords:
Elastic structures
Elastica
Bistable
Fictitious forces
Snap-through

ABSTRACT

We investigate the geometrically nonlinear deformation and buckling of a slender elastic beam subject to time-dependent 'fictitious' (non-inertial) forces arising from unsteady rotation. Using a rotary apparatus that accurately imposes an angular acceleration around a fixed axis, we demonstrate that dynamically coupled centrifugal and Euler forces can produce tunable structural deformations. Specifically, by systematically varying the acceleration ramp in a highly automated experimental setup, we show how the buckling onset of a cantilevered beam can be precisely tuned and its deformation direction selected. In a second configuration, we demonstrate that Euler forces can cause a pre-arched beam to snap-through, on demand, between its two stable states. We also formulate a theoretical model rooted in Euler's *elastica* that rationalizes the problem and provides predictions in excellent quantitative agreement with the experimental data. Our findings demonstrate an innovative approach to the programmable actuation of slender rotating structures, where complex loading fields can be produced by controlling a single input parameter, the angular position of a rotating system. The ability to predict and control the buckling behaviors under such non-trivial loading conditions opens avenues for designing devices based on rotational fictitious forces.

1. Introduction

Nearly every modern machine involves rotary elements [1] (*e.g.,* shafts, wheels, bearings, fans, and turbines), which are so ubiquitous that they often go unnoticed. Since the pioneering stud ies on rotating shafts by Rankine [2], Föppl [3], and Jeffcott [4] over a century ago, predictive modeling has become essential in designing and analyzing rotating machinery. *Rotordynamics* [5–9] has since evolved into a mature field with the primary focus of understanding the vibratory dynamics of rotating structures, to prevent large-amplitude motions that may cause catastrophic failure. Representative examples from the vast literature on rotating structures include improving the operational range and efficiency of machinery, including jet-engine turbines [10], turbo-compressors [11] and hydraulic machines [12], as well as designing centrifugal microfluidic devices [13–15] and novel space structures [16–18].

When formulating Newton's equations of motion in a rotating (non-inertial) frame of reference (FoR), three 'fictitious' body forces appear to act on a rotating body [19]: (i) the *centrifugal* force (proportional to the square of the angular velocity); (ii) the *Coriolis* force (resulting from FoR-body relative motion); and (iii) the *Euler* force (opposing angular acceleration). Unlike bulk elastic media, slender structures may undergo large, global deformations and instabilities under moderate rotational loads, making them well suited to applications in actuation, sensing, and deployable mechanisms [20]. Prior research has investigated rotation-induced instabilities in slender rods [21–24], plates [25–29], and shells [30,31]. These studies primarily considered the centrifugal forces caused by constant angular velocities, sometimes accompanied by Coriolis forces [32–34], but rarely taking the effects of Euler forces into account: in the presence of angular acceleration, it is necessary to simultaneously consider time-dependent centrifugal forces and other unsteady effects that may be present, significantly complicating analysis. As an exception, motivated by the 'spin-up' of disk drives, the stress distribution and wrinkling of unsteadily rotating elastic disks have been quantified [35,36].

Here, we perform experiments on unsteadily rotating, slender elastic beams placed eccentrically about a fixed axis (Fig. 1a–c and *Supplementary Material*, Video S1).We also conduct simulations of a dynamic model based on Euler's *elastica* [37], specialized to a rotating FoR. Two configurations are examined: cantilevered beams (clamped-free ends) and beams pre-buckled into a bistable arch (double-clamped). In both cases, the loading arises primarily from centrifugal and Euler forces. For cantilevered beams, beyond a critical angular velocity, the

* Corresponding author.
E-mail address: pedro.reis@epfl.ch (P.M. Reis).

https://doi.org/10.1016/j.eml.2024.102246
Received 16 July 2024; Received in revised form 11 October 2024; Accepted 11 October 2024
Available online 19 October 2024

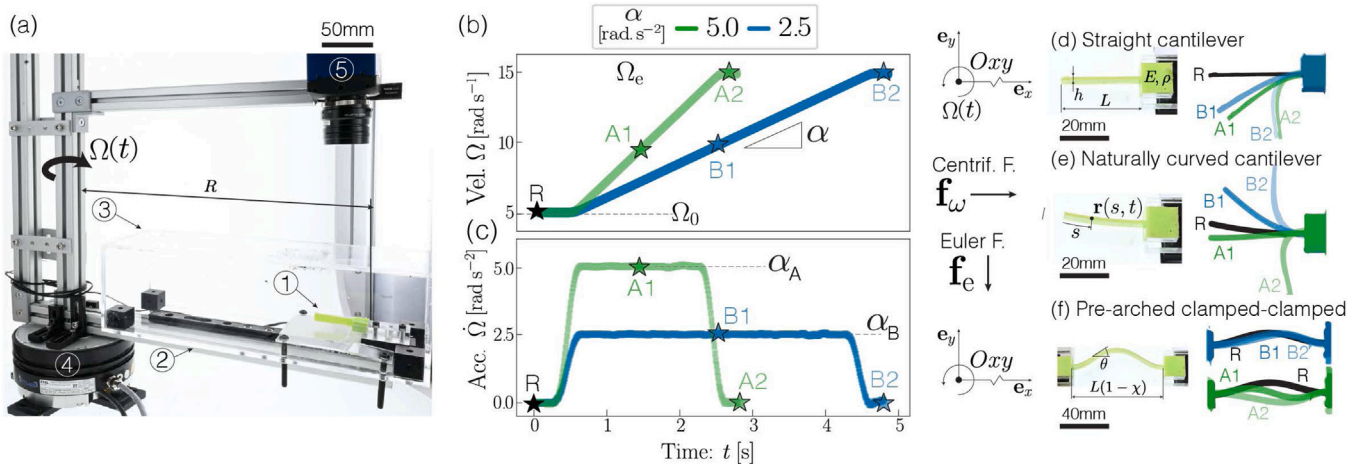

Fig. 1. Elastic beams rotating under controlled angular acceleration. (a) A beam (1) is mounted on a rigid arm (2) inside an acrylic box (3). A torque motor (4) rotates the arm and a camera (5). Right: representative time-series of (b) imposed angular velocity, $\Omega(t)$, and (c) angular acceleration, $\dot{\Omega}(t)$, with $\alpha = \{2.5, 5\}\,\mathrm{rad\,s^{-2}}$ (blue/green curves; see legend) and $(\Omega_0, \Omega_e) = (5, 15)\,\mathrm{rad\,s^{-1}}$. Bottom panels: undeformed (top row) and deformed (lower row) specimens for (d) straight and (e) naturally-curved cantilevers; and (f) pre-arched (double-clamped) beam. Deformed configurations are taken at the instances labeled in panels (b, c). See also *Supplementary Material*, Videos S1–S3. (For interpretation of the references to color in this figure legend, the reader is referred to the web version of this article.)

centrifugal force (along $+\mathbf{e}_x$; see left of Fig. 1e) triggers a buckling instability (Fig. 1d). Simultaneously, the Euler force (along $-\mathbf{e}_y$; see left of Fig. 1e) acts as a symmetry-breaking 'imperfection' that selects the buckling direction, potentially opposing the beam's natural curvature (Fig. 1e). For arched beams, these forces switch roles: the Euler force drives snap-through buckling while the centrifugal force modulates the asymmetry of the arched shape and the acceleration threshold for instability (Fig. 1f). In both cantilever and arch configurations, we show how combined centrifugal and Euler forces cause a subtle interplay between dynamic and symmetry-breaking structural effects, which can be rationalized and precisely controlled. Our study highlights how unsteady rotational loads can be leveraged for function in a new class of tunable mechanisms.

2. Experiments with controlled acceleration ramps

We perform experiments on beams cast from vinyl polysiloxane (VPS, Elite Double, Zhermack), a silicone-based elastomer: for the cantilevered beams we use VPS32 (Young's modulus $E = 1.164\,\mathrm{MPa}$, density $\rho = 1170\,\mathrm{kg\,m^{-3}}$), while for the pre-arched beams we use VPS22 ($E = 863\,\mathrm{kPa}$, $\rho = 1190\,\mathrm{kg\,m^{-3}}$) [38,39]. The casting is achieved using laser-cut acrylic molds to yield uniform, rectangular beams of width $b = 10\,\mathrm{mm}$, thickness $h \in [1.8, 2.3]\,\mathrm{mm}$, length $L \in [40, 100]\,\mathrm{mm}$ and (constant) natural curvature $\kappa_0 \in [-5, 5]\,\mathrm{m^{-1}}$. The latter range is only for the cantilevered beams; the arched beams are fabricated with no natural curvature, $\kappa_0 = 0$, prior to clamping. Each specimen is mounted onto a rigid arm attached to a high-torque motor (ETEL RTMBi140-030). An encoder records the angular position of the system at 20 kHz. The beams are clamped in the radial direction $\mathbf{e}_x$, with the outer end at a distance $R \in [350, 700]\,\mathrm{mm}$ from the center of rotation (Fig. 1a). The inner end is either free (cantilevered beams; Figs. 1d–e) or clamped at a distance $L(1-\chi)$ radially inwards from the outer end, where $\chi \in (0, 1)$ (pre-arched beams; Fig. 1f). A digital camera (Mikrotron Eosens mini1, 100–550 fps) mounted onto the rotating FoR records the deformed beams, whose centerlines are extracted via image processing. A transparent box protects each specimen against air drag.

The rotational loading is set by imposing linear ramps of the angular velocity, $\Omega(t)$ (Fig. 1b). These ramps are characterized by the initial angular velocity, Ω_0, and the plateau value α of the angular acceleration, $\dot{\Omega}(t) = \mathrm{d}\Omega/\mathrm{d}t$: we have $\dot{\Omega}(t) = \alpha$ except for short intervals at the start/end of the ramping where $\dot{\Omega}$ varies between 0 and α (Fig. 1c). Additional details on the rotation protocol are provided in Appendix A. The experimental system (motor, encoder, and camera) is fully automated, enabling a systematic exploration of parameters such as angular velocity, acceleration, and jerk.

3. Buckling of unsteadily-rotating cantilevers

First, we perform a series of experiments on rotating, straight ($\kappa_0 = 0$), cantilevered beams (Fig. 1d). The centrifugal force acts along the axis of the undeformed beam ($+\mathbf{e}_x$), exerting a compressive distributed load. Above a critical angular velocity, Ω_c, the beam buckles, causing it to bend abruptly towards $-\mathbf{e}_y$, the direction of the Euler force (Fig. 1d, right). When Ω is varied quasi-statically ($\dot{\Omega} \approx 0$), the scenario is analogous to the buckling of a vertical cantilever under increasing self-weight [22,40,41]. This gravity-induced buckling is described by a supercritical pitchfork bifurcation [42,43], as sketched in Fig. 2(a) (solid curve): as the relevant bifurcation parameter increases, the initial (undeformed) state becomes linearly unstable at the bifurcation point where two stable branches of buckled solutions emerge. We anticipate that the buckling in our rotating system also corresponds to a supercritical pitchfork bifurcation at $\Omega = \Omega_c$, but only when $\dot{\Omega} \approx 0$.

For a cantilevered beam rotated with non-negligible angular acceleration $\dot{\Omega}$, which reaches the plateau value of α (Fig. 1c), there are, *a priori*, two possible, opposing effects: (I) Due to dynamic effects, the buckling onset may occur at a *higher* Ω compared to the quasi-static scenario (dashed curve, Fig. 2a). Such delayed bifurcations are typically associated with dynamical systems involving a bifurcation parameter varied at a finite rate [44–46], as is the case with $\Omega(t)$ here. Physically, this delay arises because the system recovers from perturbations over an increasingly long timescale as it approaches the bifurcation point, thus 'lagging' behind its equilibrium value [45]. (II) Alternatively, buckling may occur at a *lower* Ω (dashed-dotted curve, Fig. 2a) due to the asymmetry (or 'imperfection') introduced by the Euler force, similar to how a transverse force (or natural curvature) lowers the buckling onset of a column under self-weight [43]. To discern whether effect (I) or (II) dominates, we vary α in the experiments while fixing all other parameters. In Fig. 2(b), we plot data for the beam's normalized midpoint deflection, $Y_\mathrm{m} = y_\mathrm{m}/L$, versus the instantaneous angular velocity, Ω, for three different accelerations, $\alpha \in \{1.5, 5.0, 10.0\}\,\mathrm{rad\,s^{-2}}$. We find that a higher α decreases the buckling onset and smooths the perfect pitchfork shape, as expected for scenario (II). This behavior is further evidenced in Fig. 2(c), which shows a 'heatmap' of Y_m versus both Ω and α. These results demonstrate that effect (II) prevails: despite the dynamic nature of the loading, the buckling instability is dominated by the symmetry-breaking effect of the Euler force. We will show below that, for cantilevered beams, the loading is quasi-static to a good approximation: the timescale of the loading is slower than the timescale over which oscillations of the beam decay, so that unsteady effects (effect I) are generally negligible.

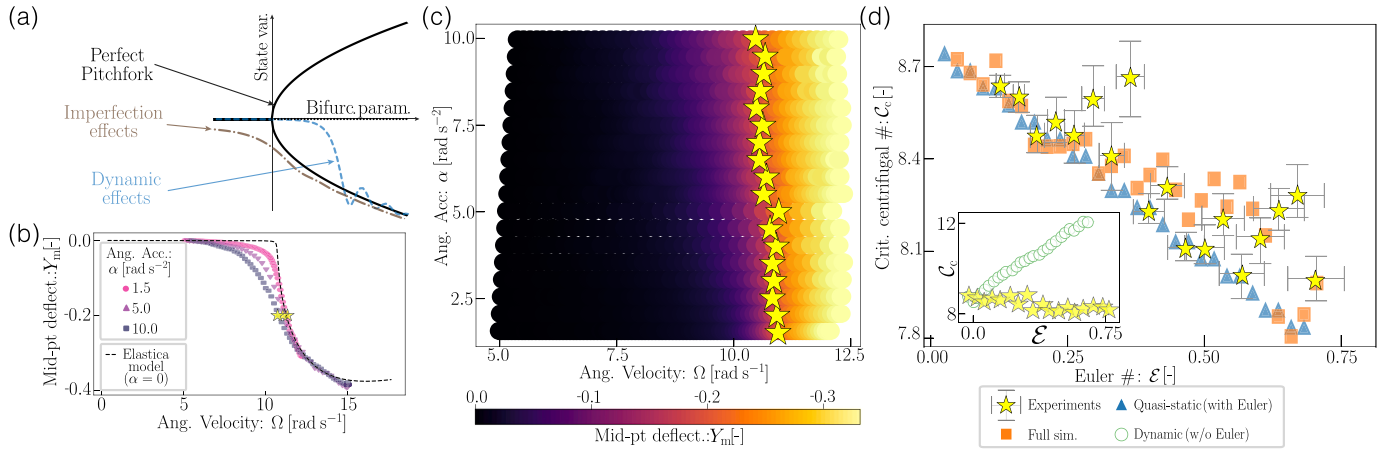

Fig. 2. Buckling of naturally straight, cantilevered beams. (a) Typical response diagrams near a supercritical pitchfork bifurcation. A 'perfect' pitchfork (black curves) is not expected for our system due to either dynamic effects (dashed curve) or symmetry-breaking imperfections (dashed-dotted curve). (b) Normalized midpoint deflection, $Y_m = y_m/L$, obtained experimentally as the angular velocity, Ω, is ramped with acceleration $\alpha = \{1.5, 5.0, 10.0\}$ rad s^{-2} (symbols; see legend). The dashed curve represents the equilibrium solution of Eqs. (4)–(5). (c) 'Heatmap' of Y_m (see colorbar) vs. Ω and α. Here, and in panel (b), stars indicate the onset of $|Y_m| \geq 0.15$. (d) Critical centrifugal number $\mathcal{C}_c$ (onset of $|Y_m| \geq 0.15$) vs. Euler number, $\mathcal{E}$, for experiments and simulations (see legend). (For interpretation of the references to color in this figure legend, the reader is referred to the web version of this article.)

4. Reduced-order model of a rotating *elastica*

Next, we formulate a geometrically nonlinear model for the elastic deformation of a beam undergoing unsteady rotation and, thus, loaded by fictitious forces. We adopt the *elastica* framework [37], albeit in a rotating FoR, to describe both a cantilevered beam (Fig. 1d–e; experimental results above) and a pre-arched beam (Fig. 1f; discussed below). These two configurations are distinguished by the respective boundary conditions (BCs) applied to the beam's inner end (free or clamped, respectively). We define Cartesian coordinates in the rotating FoR with unit vectors $\{\mathbf{e}_x, \mathbf{e}_y, \mathbf{e}_z\}$, such that the beam's outer end lies on the x-axis; see Fig. 1. Since the beam's dimensions satisfy $h \ll b \ll L$, we assume that the beam undergoes planar (x-y), inextensible, unshearable bending deformations [37]; the strains remain small but with possibly large centerline displacements. The beam is assumed to be in quasi-static moment balance since the rotational inertia of each of its elements is negligible in the limit $h \ll L$ [46].

Under the above assumptions, we represent the deformed centerline in the FoR by $\mathbf{r}(s,t) = x(s,t)\mathbf{e}_x + y(s,t)\mathbf{e}_y$, where the arclength $s \in (0, L)$ is measured from the beam's inner end (Fig. 1e). The tangent angle of the centerline, $\theta(s,t)$, is defined by $\mathbf{r}' = \cos\theta\,\mathbf{e}_x + \sin\theta\,\mathbf{e}_y$ (Fig. 1f), where we use $(\cdot)' \equiv \partial(\cdot)/\partial s$ and $\dot{(\cdot)} \equiv \partial(\cdot)/\partial t$. The centrifugal, Euler, and Coriolis forces (per unit length) experienced by the beam are, respectively, $\mathbf{f}_\omega = \rho A\Omega^2\mathbf{r}$, $\mathbf{f}_e = -\rho A\dot{\Omega}\mathbf{e}_z \times \mathbf{r}$, and $\mathbf{f}_c = -2\rho A\Omega\mathbf{e}_z \times (\dot{\mathbf{r}})_r$, where $A = bh$ is the cross-section area and $(\dot{\mathbf{r}})_r = \dot{x}\mathbf{e}_x + \dot{y}\mathbf{e}_y$ is the linear velocity in the rotating FoR; $(\cdot)_r$ denotes differentiation with respect to this frame. Writing $\mathbf{n}(s,t)$ for the resultant force, the dynamic *elastica* equations, expressing conservation of linear and angular momentum with a linearly elastic (Euler–Bernoulli) constitutive law, are [37]:

$$\mathbf{n}' + \mathbf{f}_\omega + \mathbf{f}_e + \mathbf{f}_c = \rho A\,(\ddot{\mathbf{r}})_r + \eta\,(\dot{\mathbf{r}})_r\,, \tag{1}$$

$$B\theta''\mathbf{e}_z + \mathbf{r}' \times \mathbf{n} = \mathbf{0}, \tag{2}$$

where $B = EI$ is the bending modulus, $I = h^3 b/12$ is the area moment of inertia, and we assume isotropic viscous damping (coefficient η), which lumps both external and material effects. The BCs at the outer end are $\mathbf{r}(L,t) = R\mathbf{e}_x$ and $\theta(L,t) = 0$ (Figs. 1d–f). At the inner end, we impose $\mathbf{n}(0,t) = \mathbf{0}$, $\theta'(0,t) = \kappa_0$ (cantilever), or $\mathbf{r}(0,t) = \left[R - L\,(1-\chi)\right]\mathbf{e}_x$, $\theta(0,t) = 0$ (arch). The unloaded configurations set the initial conditions.

At this point, we may estimate the relative importance of the different underlying forces (per unit length), noting that the centrifugal force scales as $|\mathbf{f}_\omega| \sim \rho A\Omega^2 R$ and the Euler force as $|\mathbf{f}_e| \sim \rho A\dot{\Omega}R$ (using $|\mathbf{r}| \sim R$). Comparing these two with the typical bending force, $|\mathbf{n}'| \sim B/L^3$, yields the dimensionless quantities:

$$\mathcal{C} = \frac{\rho A\Omega^2 R L^3}{B} \quad \text{and} \quad \mathcal{E} = \frac{\rho A\dot{\Omega}RL^3}{B}, \tag{3}$$

which we term the centrifugal and Euler numbers. Similar parameters have been identified in related problems [21,25–28,35,36], albeit with other geometric factors. The timescale of bending motions is $t^* = (\rho AL^4/B)^{1/2}$, obtained from the balance of inertial and bending forces in Eq. (1). Thus, assuming the beam deforms by a distance L over the timescale t^*, the beam velocity scales as $|(\dot{\mathbf{r}})_r| \sim L/t^*$ and the Coriolis force as $|\mathbf{f}_c| \sim \rho A\Omega L/t^*$. Using Eq. (3), we find the ratio $|\mathbf{f}_c|L^3/B = (\delta\mathcal{C})^{1/2}$, where $\delta = L/R$. Because, in general, $\mathcal{C} = O(1)$ and $\delta \ll 1$ in our experiments, the Coriolis force is negligible. Alternatively, we note that the typical magnitude of the Coriolis force can be directly compared with the centrifugal force: $|\mathbf{f}_c|/|\mathbf{f}_\omega| \sim |(\dot{\mathbf{r}})_r|/(\Omega R)$. The Coriolis force is, therefore, only significant when the beam's velocity in the FoR is comparable to the tangential velocity of the imposed rotation, which is not the case here due to the small size of the beam.

In what follows, it is advantageous to recast the dynamic elastica equations (Eqs. (1)–(2) and the geometric relation $\mathbf{r}' = \cos\theta\,\mathbf{e}_x + \sin\theta\,\mathbf{e}_y$) as a single equation involving the tangent angle θ only. This process (detailed in the *Supplementary Material*, sections S1.1–S1.2) involves integrating the geometric relation and Eq. (1) to express $\mathbf{r}$ and $\mathbf{n}$ in terms of single and double integrals involving θ, respectively; then substituting these expressions into Eq. (2) and the boundary conditions. In terms of the dimensionless arclength $S = s/L$, time $T = t/t^*$, and force components at the inner end, $\mathbf{n}(0,t) = B/L^2(P\mathbf{e}_x + Q\mathbf{e}_y)$, we obtain the following integro-differential equation for $\theta(S,T)$:

$$\begin{aligned} 0 = {} & \frac{\partial^2\theta}{\partial S^2} - (P - CS)\sin\theta + (Q + \mathcal{E}S)\cos\theta \\ & - \int_0^S \int_\xi^1 \left\{ \left[\frac{\partial^2\theta}{\partial T^2}(\sigma,T) + Y\frac{\partial\theta}{\partial T}(\sigma,T) + \delta\mathcal{E} \right] \cos\Delta\theta(S,\sigma,T) \right. \\ & \left. + \left[\frac{\partial\theta}{\partial T}(\sigma,T) + (\delta\mathcal{C})^{1/2} \right]^2 \sin\Delta\theta(S,\sigma,T) \right\} \mathrm{d}\sigma\,\mathrm{d}\xi, \end{aligned} \tag{4}$$

where we have introduced $\Delta\theta(S,\sigma,T) \equiv \theta(S,T) - \theta(\sigma,T)$ and $Y = \eta L^4/(Bt^*)$. The BCs become

$$\begin{cases} P = Q = 0, \quad \frac{\partial\theta}{\partial S}(0,T) = \tilde{\kappa}_0, \quad \theta(1,T) = 0 \quad \text{(cantilever)}; \\ \theta(0,T) = \theta(1,T) = 0, \quad \int_0^1 \begin{pmatrix} \cos\theta \\ \sin\theta \end{pmatrix} \mathrm{d}S = \begin{pmatrix} 1-\chi \\ 0 \end{pmatrix} \quad \text{(arch)}, \end{cases} \tag{5}$$

where $\tilde{\kappa}_0 = L\kappa_0$ is the dimensionless natural curvature of the beam. For arched beams, $P(T)$ and $Q(T)$ are unknown and act as Lagrange multipliers to enforce the integral constraints in Eq. (5).

The main advantage of the integro-differential formulation in Eqs. (4)–(5) is that it is more amenable to reveal the bifurcation structure of the system when working with the single unknown θ (see below). In addition, following previous work [46,47], the formulation allows for efficient dynamic simulations using the method of lines, in which we discretize the equations in space and integrate the resulting set of ordinary differential equations in time. Since we do not need to explicitly impose the inextensibility of the beam's centerline between each grid point, we avoid a large number of constraints, enabling us to integrate the discretized equations efficiently. The loading is imposed via the time-dependent centrifugal and Euler numbers defined in Eq. (3), evaluated using analytical approximations of the experimental velocity/acceleration profiles (see Appendix C). The other dimensionless parameters fixed in each experiment are the geometric ratio δ and the dimensionless damping coefficient Y. Further details on the numerical solution are provided in Appendix D.

4.1. Buckling onset: weakly nonlinear analysis

To further investigate the buckling transition observed in cantilevered beams, we perform a weakly nonlinear analysis of equilibrium solutions near the buckling onset, similar to that performed in other buckling problems [48]. We assume a small Euler number, $\mathcal{E} \ll 1$, and small natural curvature, $\tilde{\kappa}_0 \ll 1$, so that the amplitude of the solution before buckling is small: $\theta \ll 1$. We write $C^\star$ for the value of the centrifugal number C at the buckling onset (to be determined). We then perturb [48]

$$C = C^\star + \epsilon\, C^{(1)} \quad \text{and} \quad \theta = \epsilon^{1/2}\left(\theta^{(0)} + \epsilon\,\theta^{(1)} + \cdots\right), \tag{6}$$

where $\epsilon \ll 1$ is a fixed parameter (such that $\mathcal{E} = O(\epsilon^{3/2})$ and $\tilde{\kappa}_0 = O(\epsilon^{3/2})$) and $C^{(1)}$ is a control parameter. We substitute the asymptotic expansions into Eqs. (4)–(5) (neglecting time derivatives, and setting $P = Q = 0$ for cantilevered beams) and solve at successive orders in ϵ.

At $O(\epsilon^{1/2})$, we obtain the homogeneous, linear eigenvalue problem for $\theta^{(0)}(S)$ and $C^\star$:

$$\mathcal{L}\theta^{(0)} = 0, \quad \frac{\mathrm{d}\theta^{(0)}}{\mathrm{d}S}(0) = 0, \quad \theta^{(0)}(1) = 0, \tag{7}$$

$$\text{where} \quad \mathcal{L}\theta \equiv \frac{\mathrm{d}^2\theta}{\mathrm{d}S^2} + C^\star\left[S\theta - \delta\int_0^S\int_\xi^1 \Delta\theta(S,\sigma)\,\mathrm{d}\sigma\,\mathrm{d}\xi\right].$$

This determines $\theta^{(0)}$ up to an unknown (scalar) amplitude $A^{(0)}$: we can write $\theta^{(0)} = A^{(0)}\phi^{(0)}$, where $\phi^{(0)}$ satisfies Eq. (7) with normalization $\phi^{(0)}(0) = 1$. In the limit $\delta = L/R \to 0$ applicable to our experimental system, Eq. (7) is equivalent to the classical Greenhill problem for gravitational buckling [40,42], which can be solved exactly in terms of Airy functions:

$$\phi^{(0)}(S) = \frac{3^{1/6}\Gamma(2/3)}{2}\left[\sqrt{3}\,\mathrm{Ai}\left(-C^{\star\,1/3}S\right) + \mathrm{Bi}\left(-C^{\star\,1/3}S\right)\right]. \tag{8}$$

The remaining boundary condition $\phi^{(0)}(1) = 0$ then yields $\sqrt{3}\,\mathrm{Ai}(-C^{\star\,1/3}) + \mathrm{Bi}(-C^{\star\,1/3}) = 0$, the first positive root of which is $C^\star \approx 7.84$. For non-zero δ, however, the integral term in $\mathcal{L}(\cdot)$ means that an analytical solution to Eq. (7) is generally not possible. We solve the eigenvalue problem numerically (using a shooting method) to determine $\phi^{(0)}(S;\delta)$ and $C^\star(\delta)$; see *Supplementary Material*, section S2.1 for details.

At $O(\epsilon^{3/2})$, Eqs. (4)–(5) yield an inhomogeneous problem of the form (*Supplementary Material*, section S2.2)

$$\mathcal{L}\theta^{(1)} = -\left[(1-\delta)\,S + \frac{\delta}{2}S^2\right]\epsilon^{-3/2}\mathcal{E} + F\left(C^{(1)}, A^{(0)}, \phi^{(0)}, C^\star\right),$$

$$\frac{\mathrm{d}\theta^{(1)}}{\mathrm{d}S}(0) = \epsilon^{-3/2}\tilde{\kappa}_0, \quad \theta^{(1)}(1) = 0. \tag{9}$$

Because the homogeneous problem $\mathcal{L}(\cdot) = 0$ has the non-trivial solution $\phi^{(0)}$, the Fredholm Alternative Theorem [49] implies that a solution for $\theta^{(1)}$ exists only if the right-hand side of Eq. (9) satisfies a solvability condition. This solvability condition, which can be formulated by multiplying Eq. (9) by $\phi^{(0)}$ and integrating over $S \in (0,1)$, yields a cubic equation for the leading-order amplitude $A^{(0)}$:

$$0 = \epsilon^{-3/2}\left(\tilde{\kappa}_0 - c_1\mathcal{E}\right) - c_2\,C^{(1)}A^{(0)} + c_3 A^{(0)\,3}, \tag{10}$$

where c_1, c_2, and c_3 are constants that can be expressed in terms of integrals of $\phi_0(S;\delta)$ (see *Supplementary Material*, section S2.2).

When $\tilde{\kappa}_0 = 0$ and $\mathcal{E} = 0$, Eq. (10) has the form of an amplitude equation associated with a pitchfork bifurcation [50]: $A^{(0)}(c_2C^{(1)} - c_3A^{(0)\,2}) = 0$. Since the constants c_2 and c_3 are positive for $\delta \geq 0$ (*Supplementary Material*, Fig. S1), this confirms that the buckling instability is a supercritical pitchfork bifurcation at the critical centrifugal number $C^\star(\delta)$: below the buckling threshold (*i.e.*, $C^{(1)} < 0$) the only (real) solution is $A^{(0)} = 0$, while above the buckling threshold ($C^{(1)} > 0$) the non-zero (real) solutions $A^{(0)} = \pm(c_2C^{(1)}/c_3)^{1/2}$ exist.

4.2. Numerical solution compared with cantilever experiments

The weakly nonlinear analysis above is not valid when the Euler number $\mathcal{E} = O(1)$, or the system is well beyond the buckling onset so that θ is no longer small; in these cases, we must appeal to numerical solutions. For naturally straight, cantilevered beams, Fig. 2(b) shows that the computed post-buckled equilibrium branch (dashed curve) is in excellent agreement with the experiments for small but finite accelerations, serving as validation of the model.

As observed in the experimental results presented in Fig. 2(b), the buckling onset and the ensuing deformation are typically smooth in the presence of imperfections when compared to a perfect pitchfork [50]. Thus, we introduce an empirical definition for the critical centrifugal number, C_c, as the centrifugal number at which the normalized midpoint displacement first exceeds $|Y_m| = 0.15$ (stars in Figs. 2b–d). To further examine the relative importance of the different dynamic effects that are present, we probe the model and decouple the effects resulting from (I) a time-dependent angular velocity and (II) a non-zero Euler force. To do so, we either artificially omit the Euler force in Eq. (4) while keeping a time-dependent angular velocity or, instead, we ignore time-dependence by varying C quasi-statically while maintaining the Euler force. As evidenced by the data in Fig. 2(d), where we plot C_c versus $\mathcal{E}$, the full and quasi-static simulations (squares and triangles, respectively) are in agreement with the experiments (stars). (In Fig. 2d and later figures, the Euler number $\mathcal{E}$ is evaluated using Eq. (3) with $\dot{\Omega} = \alpha$, the plateau value of the acceleration during the angular velocity ramp.) By contrast, the simulations with only time-dependence of the angular velocity (circles) deviate significantly from the experiments (see inset). These results further evidence that unsteady effects are negligible compared to the 'imperfection' introduced by the Euler force, *i.e.*, (II) is the relevant scenario.

Remarkably, despite the dynamic nature of the loading, the quasi-static solution captures the experimental results in Fig. 2(d) nearly as closely as the full dynamic simulations for $\mathcal{E} \lesssim 0.3$ (corresponding to $\alpha \lesssim 3.5\ \mathrm{rad\,s^{-2}}$). This finding can be rationalized by the following scaling argument. Given an angular acceleration $\dot{\Omega}$, the timescale over which the angular velocity changes appreciably is $\sim \Omega/\dot{\Omega}$. Thus, over a timescale $t \ll \Omega/\dot{\Omega}$, the variation of Ω is negligible and Ω can be considered constant. Meanwhile, oscillations of the beam will decay sufficiently for times $t \gg [t]_d$, where $[t]_d = 2\rho A/\eta$ is the decay timescale of small-amplitude underdamped oscillations [51]. Combining these two observations, we expect that the beam is in quasi-static equilibrium for each Ω provided $\rho A/\eta \ll \Omega/\dot{\Omega}$ (or $Y^{-1} \ll \delta^{-1/2}C^{1/2}\mathcal{E}^{-1}$ in dimensionless terms). For accelerations $\dot{\Omega} = \alpha \lesssim 3.5\ \mathrm{rad\,s^{-2}}$, using $\Omega \sim 10\ \mathrm{rad\,s^{-1}}$ (the typical value at the buckling onset; see Fig. 2c)

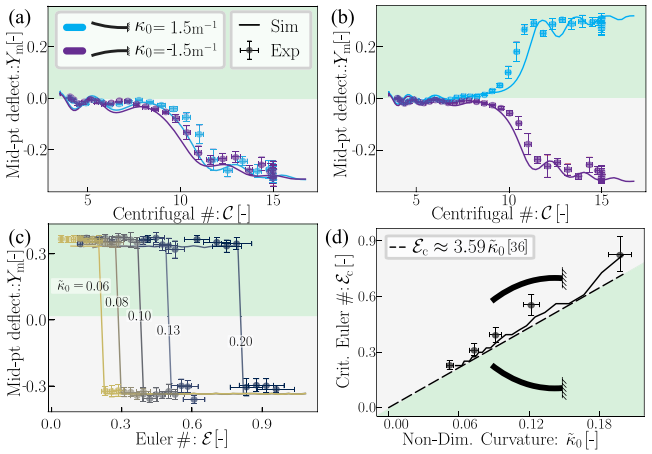

Fig. 3. Buckling of naturally curved, cantilevered beams. (The legend in (a) applies to all panels.) (a, b) Normalized midpoint deflection, $Y_m = y_m/L$, versus the centrifugal number, $\mathcal{C}$, during ramping with Euler number (a) $\mathcal{E} = 0.3$ and (b) $\mathcal{E} = 0.1$. Each panel shows data for two beams with curvatures $\kappa_0 = \pm 1.5\,\mathrm{m}^{-1}$ (purple/blue lines; see legend). See also *Supplementary Material*, Video S2. (c) Post-buckled midpoint deflection, $Y_m|_{\mathcal{C}=15}$, versus $\mathcal{E}$ for beams with dimensionless natural curvatures $\tilde{\kappa}_0 = \kappa_0/L \in \{0.06, 0.08, 0.1, 0.13, 0.2\}$. (d) Critical Euler number $\mathcal{E}_c$ (at which the buckling direction is inverted) as a function of $\tilde{\kappa}_0$. Also shown is the predicted boundary, Eq. (11), from the weakly nonlinear stability analysis (dashed line). (For interpretation of the references to color in this figure legend, the reader is referred to the web version of this article.)

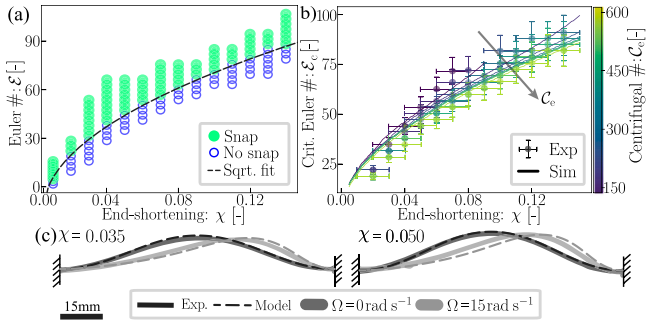

Fig. 4. Snap-through of a pre-arched (double-clamped) beam. (a) Phase diagram for the presence (closed symbols) or absence (open symbols) of snapping in the parameter space of Euler number and end-to-end shortening, $(\mathcal{E}, \chi)$ (here $\mathcal{C}_e = 373$). (b) Beam profiles obtained experimentally and numerically (solid and dashed curves, respectively) for $\chi = 0.035$ (left panel) and $\chi = 0.050$ (right). Shapes are shown at rest (dark gray) and rotating at $\Omega = 15\,\mathrm{rad\,s}^{-1}$ (light gray). (c) Critical Euler number for snapping, $\mathcal{E}_c$, versus χ at different centrifugal numbers $\mathcal{C}_e \in \{151, 198, 250, 309, 373, 445, 522, 605\}$. See also *Supplementary Material*, Video S3. (For interpretation of the references to color in this figure legend, the reader is referred to the web version of this article.)

and $\eta \approx 0.032\,\mathrm{Pa\,s}$ for our VPS32 beams (see Appendix B), we find that $\Omega/\dot{\Omega} \gtrsim 2.9\,\mathrm{s}$ and $\rho A/\eta \sim 0.67\,\mathrm{s}$, so that a quasi-static assumption is reasonable.

A detailed analysis of the midpoint trajectories during ramping indicates the presence of small oscillations due to unsteady effects. In accordance with the scaling argument above, these oscillations are usually small in magnitude so that the numerical curves closely follow the quasi-static solutions. However, the oscillation amplitudes become significant for larger accelerations, causing the discrepancy between the full dynamic simulations and the quasi-static simulations in Fig. 2(d) for $\mathcal{E} \gtrsim 0.3$. We also note that, for pre-arched beams, large oscillations occur and the quasi-static assumption is generally not satisfied due to the much larger accelerations required for snap-through (discussed below).

5. Selecting the buckling direction of curved beams

While for a straight cantilever, the centrifugal load (along $+\mathbf{e}_x$) always buckles the beam in the direction of the Euler force ($-\mathbf{e}_y$), it may be desirable in applications to pre-select the opposite buckling direction ($+\mathbf{e}_y$). This can be achieved by fabricating beams with non-zero natural curvature, κ_0 (Fig. 1e). Fig. 3(a–b) presents experimental results for two such beams possessing equal and opposite non-dimensional natural curvatures, $\tilde{\kappa}_0 = \pm 0.06$, while fixing all other parameters (experimentally, a single beam can be flipped about $\mathbf{e}_x$ before clamping). For large accelerations ($\mathcal{E} = 0.3$ in Fig. 3a; see also panels a–b in Video S2), the two cases are nearly identical, with excellent agreement between experiments and simulations, including the matching of the oscillatory nature of the curves. However, for lower accelerations ($\mathcal{E} = 0.1$ in Fig. 3b; Video S2 panels c–d), the two beams buckle in opposite directions, indicating that the geometric imperfection dominates the transverse Euler force.

To delineate the transition from a curvature-controlled to an (Euler) force-controlled buckling direction, we consider the beam's midpoint displacement, Y_m, at a fixed centrifugal number beyond buckling ($\mathcal{C} = 15$): in Fig. 3(c), this is plotted versus $\mathcal{E}$ for five beams with different dimensionless natural curvatures $\tilde{\kappa}_0 = \kappa_0/L \in [0.06, 0.2]$. As $\tilde{\kappa}_0$ is increased (*i.e.*, increasingly imperfect beams), the transition from buckling along $+\mathbf{e}_y$ (the direction of natural curvature) to $-\mathbf{e}_y$ (the direction of Euler force) occurs at higher values of $\mathcal{E}$, both in experiments (symbols) and simulations (curves). In Fig. 3(d), we plot the critical Euler number, $\mathcal{E}_c$, for this transition as a function of $\tilde{\kappa}_0$, effectively constructing a phase diagram of the beam's buckling direction. Again, there is excellent agreement between experiments (symbols) and simulations (solid curve). The variations in the solid curve are due to oscillations in the numerical trajectories, which become more pronounced for larger values of the Euler number (recall the discussion at the end of Section 4.2); close to the boundary in the phase plane, the buckling direction is highly sensitive to the interaction between these oscillations and the Euler force during ramping when the displacement starts to grow significantly. While centrifugal forces drive the buckling instability of cantilevered beams, for a given $\tilde{\kappa}_0$, the buckling direction can, therefore, be selected on-demand via accurate control of $\mathcal{E}$ according to the phase diagram in Fig. 3(d).

The phase boundary in Fig. 3(d) can also be rationalized using Eq. (10), the amplitude equation obtained from the weakly nonlinear analysis. Eq. (10) indicates that the natural curvature, $\tilde{\kappa}_0$, and Euler number, $\mathcal{E}$, behave analogously to symmetry-breaking imperfections that 'unfold' the perfect pitchfork bifurcation: for $\tilde{\kappa}_0 \neq 0$ or $\mathcal{E} \neq 0$, the amplitude $A^{(0)}$ smoothly varies from zero as $\mathcal{C}$ is quasi-statically increased past $\mathcal{C}^\star$ (meanwhile, the other buckled solution in the pair $A^{(0)} = \pm(c_2\mathcal{C}^{(1)}/c_3)^{1/2}$ forms a disconnected branch). We can infer the direction of buckling from the sign of the constant term in Eq. (10), namely $\epsilon^{-3/2}\left(\tilde{\kappa}_0 - c_1\mathcal{E}\right)$, as this term determines the sign of the amplitude $A^{(0)}$ (since $c_2 > 0$). In particular, the constant term changes sign at the critical Euler number $\mathcal{E}_c = \tilde{\kappa}_0/c_1$. While, in general, c_1 must be evaluated numerically, in the relevant limit of $\delta \to 0$, we can obtain an analytical expression using the solution for $\phi^{(0)}$ in Eq. (8). We evaluate $c_1 = 3^{-1/3}\Gamma(1/3)^{-1}\mathcal{C}^{\star -2/3}\mathrm{Ai}(-\mathcal{C}^{\star 1/3})^{-1}$ (*Supplementary Material*, section S2.2) where $\mathcal{C}^\star \approx 7.84$, and hence

$$\mathcal{E}_c = 3^{1/3}\Gamma\left(\frac{1}{3}\right)\mathcal{C}^{\star 2/3}\mathrm{Ai}\left(-\mathcal{C}^{\star 1/3}\right)\tilde{\kappa}_0 \approx 3.59\,\tilde{\kappa}_0. \tag{11}$$

Eq. (11) is used to plot the phase boundary (dashed line) in Fig. 3(d), which agrees well with the numerical and experimental results despite being formally valid only for $\mathcal{E} \ll 1$.

6. Acceleration-driven snap-through of a bistable arch

Thus far, for cantilevered beams, we showed that the centrifugal force drives buckling while the Euler force lowers the instability onset. We now turn to the pre-arched beams (Fig. 1f), for which the centrifugal and Euler forces switch roles: the latter drives snapping while

the former modulates the instability. In Fig. 4(a), we present a phase diagram for the presence/absence (closed/open symbols) of snapping in the ($\mathcal{E}$, χ) parameter space; we fix the final centrifugal number at C_e = 373 ($\Omega_e = 12\,\mathrm{rad\,s^{-1}}$). As might be expected, the phase boundary above which snapping occurs increases with the end-to-end shortening χ, corresponding to deeper arches. This phase boundary is consistent with the scaling $\mathcal{E} \sim \chi^{1/2}$ (dashed curve); an analogous scaling appears in other snap-through problems involving pre-arched beams [52], and it can be rationalized by comparing the typical midpoint deflection (here due to Euler forces) to the initial arch height. We have thus demonstrated the possibility of actuating rotating mechanisms via the Euler force, whose acting direction can be selected. Euler-actuated mechanisms may switch reversely between stable states, unlike if actuated alone by centrifugal forces, which always act radially outwards.

Although the centrifugal force does not drive snapping, the arch shape becomes increasingly asymmetric when driven at higher angular velocities due to the centrifugal force (Fig. 4c). Naively, one might expect that this asymmetry would tend to increase the total bending energy, thereby significantly decreasing the energetic barrier for snapping (and hence $\mathcal{E}_c$). In Fig. 4(b) we explore the effect of the centrifugal load, C_e, on the critical Euler number for snapping, $\mathcal{E}_c$, again plotted as a function of end-to-end shortening, χ. Surprisingly, we observe only a modest reduction of $\mathcal{E}_c$ with C_e, in particular for higher values of χ when the shape asymmetry may be large. It is important to note that for the control stability of the motor, we impose loading profiles with finite and constant jerk across experiments (see Appendix A). This imposition places a physical limit on the maximum achievable angular acceleration for a given velocity change. Consequently, at high levels of compression χ, it is generally not possible to generate sufficient Euler forces to induce beam snapping. This physical constraint limits our ability to fully explore the effects of angular velocity in cases with large χ, where one might expect more pronounced effects of shape asymmetry. Overall, these results demonstrate that although the angular velocity does not have a major impact on the critical snap-through load, an accurate angular velocity control can both trigger and modify the snapping of a pre-arched beam.

7. Conclusions

In conclusion, we demonstrated the feasibility of leveraging both centrifugal and Euler forces to precisely trigger and tune, on-demand, instabilities in rotating *elastica* structures by accurately controlling their angular velocity drive. Looking ahead, our investigation can be broadened to include more complex loading profiles (*e.g.*, harmonic velocities), diverse geometries (*e.g.*, tapered beams, plates, and shells), varying material properties (*e.g.*, nonlinear and metamaterial behavior), and different boundary conditions (*e.g.*, pins or roller-springs whose position depends on the centrifugal force). While for our cantilevered beams, we found that the loading is approximately quasi-static, future efforts should address the conditions under which the unsteady effects (effect I) dominate. Even speculatively, we envisage that the understanding developed here will find practical application in a variety of systems involving unsteady rotations, particularly where functionality is achieved through the active actuation of embedded components. Examples include acceleration-actuated operators for centrifugal microfluidic cartridges and automated quality testing of micro-components via complex loading protocols. At larger scales, our insights into the structural effects of Euler forces may contribute to the development of turbines capable of better operating under unsteady regimes and also in aerospace, enabling the design of mechanical switches that are actuated by accelerations encountered during orbital changes. Thus, the advances offered by the present study offer the potential to pave the way for a new class of 'programmable' mechanisms that harness the rich instabilities inherent to unsteadily rotating structures, a novel conceptional framework applicable to generic rotating systems.

CRediT authorship contribution statement

Eduardo Gutierrez-Prieto: Writing – review & editing, Writing – original draft, Visualization, Validation, Methodology, Investigation, Formal analysis, Data curation, Conceptualization. **Michael Gomez:** Writing – review & editing, Writing – original draft, Validation, Software, Methodology, Investigation, Formal analysis. **Pedro M. Reis:** Writing – review & editing, Supervision, Resources, Project administration, Methodology, Investigation, Funding acquisition, Formal analysis, Conceptualization.

Declaration of competing interest

The authors declare that they have no known competing financial interests or personal relationships that could have appeared to influence the work reported in this paper. We note that we have recently filed a patent application connected to this manuscript with the European Patent Office, The Hague, Netherlands. PCT Application number: PCT/EP2024/054220

Declaration of Generative AI and AI-assisted technologies in the writing process

During the preparation of this work, the authors used ChatGPT (3.5 & 4) and Grammarly in order to improve the readability and to ensure grammatical correctness of the manuscript. After using this tool/service, the authors reviewed and edited the content as needed and take full responsibility for the content of the published article.

Appendix A. Rotation protocol

The rotational loading is set by imposing a time-dependent angular velocity, $\Omega(t)$, in two stages. First, in a pre-loading stage, $\Omega(t)$ is slowly ramped from zero to $\Omega_0 > 0$ at an acceleration $\dot{\Omega} = 5\,\mathrm{rad\,s^{-2}}$, before being held at Ω_0 for 2s, ensuring the decay of any transient oscillations. Next, in the second loading stage, $\Omega(t)$ is ramped from Ω_0 to Ω_e (where $\Omega_e > \Omega_0$); throughout this stage, the angular acceleration is constant, $\dot{\Omega} = \alpha$, except for short 'jerk intervals' (duration $t_j = 100$ ms) at the start/end of the ramping when $\dot{\Omega}$ rapidly varies between α and zero. Two representative time series of $\Omega(t)$ and $\dot{\Omega}(t)$ are presented in Fig. 1(b) and Fig. 1(c), respectively. The error bars associated with the experimental data are calculated considering the uncertainty of the beam's material properties and geometry, the pixel size and resolution of the imaging system, and uncertainty in the angular position output by the motor encoder. Besides, the error bars of the centrifugal and Euler numbers consider the standard deviation of the measured angular velocity between recorded frames since the temporal resolution of the encoder (20 kHz) is much larger than the recording framerate (100–550 Hz).

Appendix B. Damping coefficient characterization

The value of the damping coefficient η used in our model was measured from underdamped oscillations of the beams (in a cantilevered configuration) in the absence of rotational loading. According to linear stability analysis, small-amplitude underdamped oscillations decay in time like $e^{-t/[t]_d}$, where the time constant is $[t]_d = 2\rho A/\eta$ [51]. Experimentally, we perturbed the beams and extracted the time series of the tip displacement; the time constant $[t]_d$ was then determined by fitting the envelope of the oscillations. Using the known values of ρ and A (see main text), we obtain $\eta = (0.032 \pm 0.003)\,\mathrm{Pa\,s}$ and $\eta = (0.043 \pm 0.003)\,\mathrm{Pa\,s}$ for the beams fabricated using VPS32 and VPS22, respectively.

Appendix C. Rotational loading model

In our dimensionless model, Eqs. (4)–(5), the rotational loading is imposed via the time-dependent centrifugal number, $\mathcal{C}$, and Euler number, $\mathcal{E}$, defined in Eq. (3). To evaluate $\mathcal{C}$ and $\mathcal{E}$, we use analytical expressions for $\Omega(t)$ and $\dot{\Omega}(t)$ that approximate the angular velocity and acceleration imposed experimentally. In particular, we simulate the two dynamic stages (pre-loading and loading) as described above (Rotation protocol). During the second (loading) stage, we approximate the angular acceleration during each jerk interval using the so-called *smootherstep* function [53], denoted S_2. For a general quantity $a(t)$, this function is a monotonic ramp between the points $(a,t) = (a_0,t_0)$ and (a_1,t_1), with zero first and second-order derivatives at the end-points:

$$S_2(t;t_0,t_1,a_0,a_1) = a_0 + (a_1-a_0)\left(6\tau^5 - 15\tau^4 + 10\tau^3\right),$$
$$\text{where} \quad \tau = \frac{t-t_0}{t_1-t_0} \in (0,1).$$

With Δt denoting the duration of the loading stage (taken to start at $t=0$), the angular acceleration during the loading stage is modeled as the piece-wise function

$$\dot{\Omega}(t) = \begin{cases} S_2(t;0,t_j,0,\alpha) & 0 \le t < t_j, \\ \alpha & t_j \le t < \Delta t - t_j, \\ S_2(t;\Delta t - t_j,\Delta t,\alpha,0) & \Delta t - t_j \le t < \Delta t. \end{cases}$$

The corresponding angular velocity, $\Omega(t)$, can be determined by integration using the initial condition $\Omega(0) = \Omega_0$. The angular velocity at the end of the loading stage is then $\Omega(\Delta t) = \Omega_0 + \alpha(\Delta t - t_j)$. Thus, to satisfy the imposed final value $\Omega(\Delta t) = \Omega_e$, we choose $\Delta t = \left(\Omega_e - \Omega_0\right)/\alpha + t_j$.

Appendix D. Numerical solutions

We define a uniform mesh on $S \in [0,1]$ with spacing $\Delta S = 1/N$ (so that there are $N+1$ grid points in total). Our discretization of Eqs. (4)–(5) on this mesh follows that employed previously by Refs. [46,47] to simulate the snap-through dynamics of an *elastica*. We formulate a scheme with second-order accuracy as $\Delta S \to 0$: we approximate the $\partial^2\theta/\partial S^2$ term in Eq. (4) using a second-order centered difference on the numerical mesh, and we use the trapezium rule to approximate integrals. The resulting system of ODEs is written in matrix–vector form and integrated using the solver `ode15s` in MATLAB. For pre-arched beams, the integral constraints in Eq. (5) mean that the system is differential–algebraic (since the Lagrange multipliers P and Q do not explicitly appear in the integral constraints). This can be avoided using the method described in Ref. [54]: we differentiate the integral constraints twice in time, then eliminate $\partial^2\theta/\partial T^2$ terms (using the discretized form of Eq. (4)) to obtain a closed linear system for P and Q. In all simulations reported in the main text, we take $N = 100$, having checked that the results are insensitive to increasing N or decreasing integration tolerances. Each simulation typically completes in a few seconds on a laptop computer.

At the start of the pre-loading stage, the beam is at rest and in equilibrium in the absence of external loads, $\mathcal{C} = \mathcal{E} = 0$. For cantilevered beams, the beam is stress-free in this equilibrium and everywhere adopts its natural curvature $\tilde{\kappa}_0$, i.e., $\theta(S) = -\tilde{\kappa}_0(1-S)$. (This may be verified as the equilibrium solution of Eqs. (4)–(5) when $\mathcal{C} = \mathcal{E} = 0$.) In the case of pre-arched beams (with $\tilde{\kappa}_0 = 0$), the beam undergoes Euler (pre-)buckling in the absence of external loads due to the imposed end-to-end shortening, χ, between the double-clamped boundaries. To determine the beam shape, we solve numerically the steady version of Eqs. (4)–(5) (with $\mathcal{C} = \mathcal{E} = 0$). This is achieved by discretizing the equations (in an identical manner to our dynamic simulations) and solving the resulting set of algebraic equations in MATLAB using the routine `fsolve`. As an initial guess, we use the linearized solution for $\theta \ll 1$ corresponding to mode-1 Euler buckling:

$$\theta(S) = 2\chi^{1/2}\sin(2\pi S).$$

Appendix E. Supplementary data

Supplementary material related to this article can be found online at https://doi.org/10.1016/j.eml.2024.102246.

Data availability

Data will be made available on request.

References

[1] J.E. Shigley, L.D. Mitchell, H. Saunders, Mechanical Engineering Design (4th Ed.), J. Mech. Transm. Autom. Des. 107 (2) (1985) 145, http://dx.doi.org/10.1115/1.3258702.

[2] W.J.M. Rankine, On the centrifugal force of rotating shafts, Engineer 27 (1869) 249.

[3] A. Föppl, Das problem der lavalschen turbinenwelle, Der Civilingenieur 4 (1895) 335–342.

[4] H.H. Jeffcott, The lateral vibration of loaded shafts in the neighbourhood of a whirling speed.—The effect of want of balance, Phil. Mag. 37 (219) (1919) 304–314.

[5] J.S. Rao, History of Rotating Machinery Dynamics, Springer Science & Business Media, Berlin, Germany, 2011.

[6] D. Childs, Turbomachinery Rotordynamics: Phenomena, Modeling, and Analysis, John Wiley & Sons, Hoboken, NJ, 1993.

[7] A.D. Dimarogonas, S.A. Paipetis, T.G. Chondros, Analytical methods in rotor dynamics, Springer Science & Business Media, 2013.

[8] A. Muszynska, Rotordynamics, CRC Press, 2005.

[9] G. Genta, Dynamics of rotating systems, Springer Science & Business Media, 2005.

[10] A.V. Srinivasan, Flutter and Resonant Vibration Characteristics of Engine Blades, J. Eng. Gas Turbines Power. 119 (4) (1997) 742–775, http://dx.doi.org/10.1115/1.2817053.

[11] T. Verstraete, Z. Alsalihi, R.A. Van den Braembussche, Multidisciplinary Optimization of a Radial Compressor for Microgas Turbine Applications, J. of Turbomach. 132 (031004) (2010) http://dx.doi.org/10.1115/1.3144162.

[12] J. Gomes Pereira, E. Vagnoni, A. Favrel, C. Landry, S. Alligné, C. Nicolet, et al., Prediction of unstable full load conditions in a Francis turbine prototype, Mech. Syst. Signal Process. 169 (2022) 108666, http://dx.doi.org/10.1016/j.ymssp.2021.108666.

[13] R. Gorkin, J. Park, J. Siegrist, M. Amasia, B. Seok Lee, J.-M. Park, et al., Centrifugal microfluidics for biomedical applications, Lab Chip 10 (14) (2010) 1758–1773, http://dx.doi.org/10.1039/B924109D.

[14] L.X. Kong, A. Perebikovsky, J. Moebius, L. Kulinsky, M. Madou, Lab-on-a-CD: A Fully Integrated Molecular Diagnostic System, J. Lab. Autom. 21 (3) (2016) 323–355, http://dx.doi.org/10.1177/2211068215588456.

[15] M.S. Bhamla, B. Benson, C. Chai, G. Katsikis, A. Johri, M. Prakash, Hand-powered ultralow-cost paper centrifuge, Nat. Biomed. Eng. 1 (1) (2017) 0009.

[16] H. Moravec, A non-synchronous orbital skyhook, J. Astronaut. Sci. 25 (1977) 307–322.

[17] R. Wu, P.C.E. Roberts, C. Soutis, C. Diver, Heliogyro solar sail with self-regulated centrifugal deployment enabled by an origami-inspired morphing reflector, Acta Astronaut. 152 (2018) 242–253, http://dx.doi.org/10.1016/j.actaastro.2018.08.012.

[18] M. Gardsback, G. Tibert, Deployment control of spinning space webs, J. Guid. Control Dyn. 32 (1) (2009) 40–50.

[19] P.A. Tipler, G.P. Mosca, Physics for Scientists and Engineers, vol. 1, W. H. Freeman and Company, New York, NY, 2002.

[20] P.M. Reis, A Perspective on the Revival of Structural (In)Stability With Novel Opportunities for Function: From Buckliphobia to Buckliphilia, J. Appl. Mech. 82 (11) (2015) 111001, http://dx.doi.org/10.1115/1.4031456.

[21] N. Mostaghel, I. Tadjbakhsh, Buckling of rotating rods and plates, Int. J. Mech. Sci. 15 (6) (1973) 429–434, http://dx.doi.org/10.1016/0020-7403(73)90026-X.

[22] W.F. White, R.G. Kvaternik, K.R.V. Kaza, Buckling of rotating beams, Int. J. Mech. Sci. 21 (12) (1979) 739–745, http://dx.doi.org/10.1016/0020-7403(79)90054-7.

[23] I. Aganović, J. Tambača, On the Stability of Rotating Rods and Plates, J. Appl. Math. Mech. 81 (11) (2001) 733–742, http://dx.doi.org/10.1002/1521-4001(200111)81:11<733::AID-ZAMM733>3.0.CO;2-8.

[24] F. Richard, A. Chakrabarti, B. Audoly, Y. Pomeau, S. Mora, Buckling of a spinning elastic cylinder: linear, weakly nonlinear and post-buckling analyses, Proc. R. Soc. A 474 (2216) (2018) 20180242, http://dx.doi.org/10.1098/rspa.2018.0242.

[25] J.L. Nowinski, Nonlinear transverse vibrations of a spinning disk, J. Appl. Mech. 31 (1) (1964) 72–78, http://dx.doi.org/10.1115/1.3629573.

[26] J.-S. Chen, Y.-Y. Chang, On the unsymmetrical deformation and reverse snapping of a spinning non-flat disk, Int. J. Non-Linear Mech. 42 (8) (2007) 1000–1009.

[27] J.-S. Chen, Y.-Y. Fang, Warping of stationary and rotating heavy disks, Int. J. Solids Struct. 48 (21) (2011) 3032–3040.
[28] M. Delapierre, D. Chakraborty, J.E. Sader, S. Pellegrino, Wrinkling of transversely loaded spinning membranes, Int. J. Solids Struct. 139–140 (2018) 163–173, http://dx.doi.org/10.1016/j.ijsolstr.2018.01.031.
[29] C.D. Coman, Wrinkling of a normally loaded, spinning, elastic membrane: An asymptotic approximation, Int. J. Non-Linear Mech. 156 (2023) 104482, http://dx.doi.org/10.1016/j.ijnonlinmec.2023.104482.
[30] K.Y. Lam, C.T. Loy, Analysis of rotating laminated cylindrical shells by different thin shell theories, J. Sound Vib. 186 (1) (1995) 23–35, http://dx.doi.org/10.1006/jsvi.1995.0431.
[31] H. Li, K.-Y. Lam, T.-Y. Ng, Rotating Shell Dynamics, Elsevier, Amsterdam, Netherlands, 2005.
[32] S.P. Sane, A. Dieudonné, M.A. Willis, T.L. Daniel, Antennal Mechanosensors Mediate Flight Control in Moths, Science 315 (5813) (2007) 863–866, http://dx.doi.org/10.1126/science.1133598.
[33] S. Sreenivasamurthy, V. Ramamurti, Coriolis effect on the vibration of flat rotating low aspect ratio cantilever plates, J. Strain Anal. Eng. Des. 16 (2) (1981) 97–106, http://dx.doi.org/10.1243/03093247V162097.
[34] J.R. Banerjee, D. Kennedy, Dynamic stiffness method for inplane free vibration of rotating beams including coriolis effects, J. Sound Vib. 333 (26) (2014) 7299–7312, http://dx.doi.org/10.1016/j.jsv.2014.08.019.
[35] S. Tang, Note on acceleration stress in a rotating disk, Int. J. Mech. Sci. 12 (2) (1970) 205–207, http://dx.doi.org/10.1016/0020-7403(70)90020-2.
[36] J.E. Sader, M. Delapierre, S. Pellegrino, Shear-induced buckling of a thin elastic disk undergoing spin-up, Int. J. Solids Struct. 166 (2019) 75–82, http://dx.doi.org/10.1016/j.ijsolstr.2019.01.038.
[37] B. Audoly, Y. Pomeau, Elasticity and Geometry: From Hair Curls to the Non-linear Response of Shells, Oxford University Press, Oxford, UK, 2010.
[38] P. Grandgeorge, T.G. Sano, P.M. Reis, An elastic rod in frictional contact with a rigid cylinder, J. Mech. Phys. Solids 164 (2022) 104885, http://dx.doi.org/10.1016/j.jmps.2022.104885.
[39] P. Leroy-Calatayud, M. Pezzulla, A. Keiser, K. Mulleners, P.M. Reis, Tapered foils favor traveling-wave kinematics to enhance the performance of flapping propulsion, Phys. Rev. Fluids 7 (7) (2022) 074403, http://dx.doi.org/10.1103/PhysRevFluids.7.074403.
[40] M.A. Greenhill, Determination of the greatest height consistent with stability that a vertical pole or mast can be made, and of the greatest height to which a tree of given proportions can grow, Camb. Phil. Soc. Proc. 4 (1881) 65–73.
[41] J.M.T. Thompson, On the simulation of a gravitational field by a centrifugal field, Int. J. Mech. Sci. 13 (12) (1971) 979–986.
[42] C.Y. Wang, A critical review of the heavy elastica, Int. J. Mech. Sci. 28 (8) (1986) 549–559.
[43] L.N. Virgin, R.H. Plaut, Postbuckling and vibration of linearly elastic and softening columns under self-weight, Int. J. Solids Struct. 41 (18–19) (2004) 4989–5001.
[44] J. Su, The phenomenon of delayed bifurcation and its analyses, in: C.K.R.T. Jones, A.I. Khibnik (Eds.), Multiple-Time-Scale Dynamical Systems, Springer, New York, NY, 2001, pp. 203–214.
[45] J.R. Tredicce, G.L. Lippi, P. Mandel, B. Charasse, A. Chevalier, B. Picqué, Critical slowing down at a bifurcation, Am. J. Phys. 72 (6) (2004) 799–809.
[46] M. Liu, M. Gomez, D. Vella, Delayed bifurcation in elastic snap-through instabilities, J. Mech. Phys. Solids 151 (2021) 104386.
[47] M. Gomez, Ghosts and bottlenecks in elastic snap-through (Ph.D. thesis), University of Oxford, 2018.
[48] P. Howell, G. Kozyreff, J. Ockendon, Applied Solid Mechanics, Cambridge University Press, Cambridge, UK, 2009.
[49] J.P. Keener, Principles of Applied Mathematics: Transformation and Approximation, CRC Press, Boca Raton, FL, 1988.
[50] S.H. Strogatz, Nonlinear Dynamics and Chaos, Westview Press, Boulder, CO, 2015.
[51] Z.P. Bažant, L. Cedolin, Stability of Structures: Elastic, Inelastic, Fracture and Damage Theories, World Scientific, 2010.
[52] M. Gomez, D.E. Moulton, D. Vella, Passive control of viscous flow via elastic snap-through, Phys. Rev. Lett. 119 (14) (2017) 144502.
[53] D.S. Ebert, F.K. Musgrave, D. Peachey, K. Perlin, S. Worley, Texturing & modeling: a procedural approach, Morgan Kaufmann, 2003.
[54] P.T. Ruhoff, E. Præstgaard, J.W. Perram, Efficient algorithms for simulating complex mechanical systems using constraint dynamics, Proc. R. Soc. A 452 (1948) (1996) 1139–1165.